HHS Public Access

Author manuscript

Nat Biotechnol. Author manuscript; available in PMC 2015 June 01.

Published in final edited form as:

Nat Biotechnol. 2014 December ; 32(12): 1268–1275. doi:10.1038/nbt.3044.

A load driver device for engineering modularity in biological networks

Deepak Mishra[1,2], **Phillip M. Rivera-Ortiz**[2,3], **Allen Lin**[2,5], **Domitilla Del Vecchio**[2,3,4,*], and **Ron Weiss**[1,2,5,*]

[1]Department of Biological Engineering, Massachusetts Institute of Technology, Cambridge, MA, USA

[2]Synthetic Biology Center, Massachusetts Institute of Technology, Cambridge, MA, USA

[3]Department of Mechanical Engineering, Massachusetts Institute of Technology, Cambridge, MA, USA

[4]Laboratory for Information and Decision Systems, Massachusetts Institute of Technology, Cambridge, MA, USA

[5]Department of Electrical Engineering/Computer Science, Massachusetts Institute of Technology, Cambridge, MA, USA

Abstract

The behavior of gene modules in complex synthetic circuits is often unpredictable[1–4]. Upon joining modules to create a circuit, downstream elements (such as binding sites for a regulatory protein) apply a load to upstream modules that can negatively affect circuit function[1,5]. Here we devise a genetic device named a load driver that mitigates the impact of load on circuit function, and we demonstrate its behavior in *Saccharomyces cerevisiae*. The load driver implements the design principle of time scale separation: inclusion of the load driver's fast phosphotransfer processes restores the capability of a slower transcriptional circuit to respond to time-varying input signals even in the presence of substantial load. Without the load driver, we observe circuit behavior that suffers from 76% delay in response time and a 25% decrease in system bandwidth due to load. With the addition of a load driver, circuit performance is almost completely restored. Load drivers will serve as fundamental building blocks in the creation of complex, higher level genetic circuits.

Understanding the limits of modularity in biological systems and developing appropriate mechanisms to overcome these limitations is an important challenge in the design and construction of synthetic systems[6–8]. Modularity can fail at different levels of the system

*Correspondence to: rweiss@mit.edu (R.W.) and ddv@mit.edu (D.D.V.).

D.M., D.D.V., and R.W. designed the experiments and analyzed the data. D.M. performed the experiments. P.M.R constructed mathematical models and performed parameter estimation. A.L. cloned constructs. D.M., D.D.V., and R.W. wrote the paper. Sequences for pLDUNB, pLDBUF, pLDBUFL, pLD00X, PLD01X, and pLD02X are available from GenBank (*Accession IDs Pending*). All materials (plasmids, strains) are available upon request. The authors declare that they have no competing financial interests.

hierarchy. Examples include interference between promoter and transcript regions due to structural interactions between DNA and RNA or proteins, or functional interactions with host factors and metabolites[9]. At the genetic parts level, it has been shown recently that promoter-transcript interference can be addressed by cleaving a transcript through the addition of so-called insulators such as ribozymes[6] or CRISPR-mediated cleavage[7]. Modularity failures at the circuit topology level, however, have not yet been addressed. At this level, protein signals from devices or modules such as an oscillator[10,11], a toggle switch[12], or an activation cascade[13] can serve as input and output signals to perform human-defined regulatory functions[14]. For building complex multi-module circuits, it is desirable that module behavior (as characterized individually) does not change substantially when creating functional connections to other modules.

One common method for engineering a connection between an upstream and a downstream module in transcriptional networks is to have the upstream module's output protein bind DNA operator sites in promoters of the downstream module. Analogously, modules in engineered protein networks can be connected through protein docking domains. Reversible binding reactions between upstream regulatory proteins and downstream binding sites (e.g. DNA operators or protein docking domains) create load that can temporarily sequester the regulatory proteins from other reactions, resulting in undesirable delays or disruptions in system function. Loads have dramatic effects on system behavior and these effects are known as retroactivity[5,15–19].

Retroactivity has been detected in both natural and synthetic biological systems. In the endogenous *Drosophila* MAPK pathway, phosphorylation levels of the upstream Ras/ERK module are perturbed by concentration changes of downstream substrates Cic and Gro, resulting in retroactive effects that contribute to spatial regulation of early embryonic gene expression[15,20]. Experiments on a reconstituted PII/NRII signal transduction cascade of *E. coli* in a cell-free environment demonstrated that downstream NRII targets dramatically affect the upstream (UTase/UR)-PII cycle's temporal response[16]. While natural systems encode network topologies that function despite retroactivity, or may sometimes exploit it[15,20], design of synthetic networks is often confounded by retroactivity. Experiments with synthetic networks in *E. coli* validate the undesirable impact of retroactivity, such as in a transcriptional repression cascade whose temporal response is substantially affected by addition of a downstream module encoding transcription factor target operators[17]. Another experiment in *E. coli* showed that the steady state input/output characteristic of an upstream repressor module significantly changes when a downstream system with the repressor's binding sites is added[18]. Therefore, creation of large-scale synthetic transcriptional networks will be difficult without design strategies that overcome problems of modular composition.

To mitigate retroactivity, we report the design and implementation of a load driver, a fast phosphotransfer-based device that is placed between slower upstream and downstream transcriptional modules (Figs. 1A, 1B). Incorporation of fast processes as a bridge between slower processes exemplifies the design principle of time scale separation to insulate an upstream module from load applied by its downstream module[21]. The load driver design principle was obtained by mathematically formulating the issue of load as a control theoretic problem of disturbance attenuation[21] (Supplementary Note §1.1, 1.2). In Box 1, we provide

simplified analysis of how separation of time scale is used to attenuate retroactivity. By virtue of its fast dynamics, the load driver responds almost instantaneously to the slower temporal changes in its input and quickly reaches a quasi-steady state (QSS), such that the comparatively slower changing input seems constant. Load from the downstream module is transferred to the load driver's output and can affect both the time needed to reach QSS and the QSS itself. First, since the load driver's dynamics are very fast, any load-induced delays in reaching the QSS occur at the faster time scale. Hence, delays are negligible relative to the slower operation of the flanking modules. Second, key regulatory elements of the load driver are sufficiently abundant such that the QSS is unaffected by load, as illustrated below and in Supplementary Note §1.1. The combined effect is that the load driver mitigates retroactivity and the operation of the upstream and downstream module is independent of their connectivity.

To experimentally characterize the load driver's performance in attenuating retroactivity, we designed and integrated four system types (Fig. 1C–E) into *Saccharomyces cerevisiae*. All four systems have identically functioning upstream modules with doxycycline (DOX) as input, and an output module containing green fluorescent protein (GFP) as output. The systems differ in whether they include a load module and a load driver. The upstream modules contain constitutively expressed reverse tetracycline transactivator protein (rtTA) which induces P_{TET} promoter expression in the presence of DOX. Unbuffered systems do not include the load driver and the upstream module is connected directly to the output module and, if present, the load module (Fig 1D). In the buffered systems, we introduce an intervening load driver module that incorporates a phosphotransfer cascade between the upstream and output modules (Fig 1E). Comparison of circuit behaviors with and without the load module in both systems allowed us to determine the load driver's ability to attenuate retroactivity.

In the unbuffered system (Fig. 1D, Supplementary Fig. 1), P_{TET} regulates expression of SKN7m, a constitutively active phosphorylated mutant of the nuclear aspartate response regulator SKN7[22]. SKN7m activates expression of GFP from the synthetic promoter $P_{TR\text{-}SSRE}$[23] to provide an output readout in response to DOX input. All system elements are chromosomally integrated except for the load variants, which are encoded on high-copy 2μ yeast plasmids (50–100 copies/cell)[24] each with either zero (unloaded), one (single-loaded), or two (double-loaded) additional copies of $P_{TR\text{-}SSRE}$ (Supplementary Figs. 1, 2). The load creates reversible binding reactions between SKN7m and corresponding operators within $P_{TR\text{-}SSRE}$, resulting in additional flux (retroactivity) that affects the rate of change of SKN7m available to activate the output[5,17]. For the unbuffered circuits, upon induction with DOX the *total* amount of SKN7m increases with time but a portion binds $P_{TR\text{-}SSRE}$ operators, slowing down the increase of *free* SKN7m available to activate system output.

In the buffered systems (Fig. 1E, Supplementary Fig. 1), DOX binds rtTA and induces expression of a novel fusion protein, STAT5-HKRR, comprising murine signal transducer and activator of transcription 5 (STAT5) fused to the histidine kinase (HK) and response regulator (RR) domains of the yeast synthetic lethal to N-end rule protein (SLN1). This protein, described in the methods, serves as input to the load driver. Within the load driver, a protein that consists of the JH1 domain from murine Janus kinase 2 (JAK2) is constitutively

expressed. This JH1 domain autophosphorylates before phosphorylating the STAT5 domain of STAT5-HKRR, resulting in dimerization of STAT5-HKRR[25]. STAT5 mediated dimerization enables HK auto-phosphorylation, phosphotransfer to the RR domain, and subsequent phosphotransfer to constitutively expressed tyrosine phosphate dependent protein (YPD1). Upon activation, two phospho-YPD1 proteins reversibly transfer their phosphates to constitutively expressed SKN7 to form doubly-phosphorylated SKN7[22,26]. Phospho-SKN7 activates expression of GFP from chromosomally integrated $P_{TR\text{-}SSRE}$ and also binds plasmid-encoded load sites. Whereas the input module's output protein (SKN7m) in the unbuffered systems binds $P_{TR\text{-}SSRE}$ directly, the corresponding protein (SKN7) in the buffered systems' load driver module requires activation by a sequence of phosphotransfer reactions before binding $P_{TR\text{-}SSRE}$.

To analyze the overall design and crucial components for operation of our load driver, we developed a detailed mathematical model based on mass-action kinetics and Ordinary Differential Equations (ODEs) (Supplementary Note §1.3). This analysis shows that sufficiently large phosphotransfer rates ensure the time scale separation required for quickly reaching the QSS, and sufficiently high concentrations of SKN7 and YPD1 render this QSS independent of load (Supplementary Note §1.4 – 1.6). Specifically, large amounts of these proteins guarantee that the steady state sequestration of phospho-SKN7 by the promoter binding sites can be effectively compensated by activation of additional SKN7 (Supplementary Note §1.6.4). We chose to make two versions of the buffered system (Fig. 1E) with one version encoding promoters expressing SKN7 and YPD1 with relatively low expression levels and a second version encoding promoters expressing these proteins with moderate wild-type expression levels. This and several additional design choices in the creation of our experimental systems are described in the methods.

For our initial experimental characterization, we conducted time-series experiments with a single step input change applied to all systems. DOX was introduced to log-phase liquid cultures without prior inducer (step-up) or removed from cultures previously grown in saturating inducer (step-down). For the step-up experiment, the loaded unbuffered system exhibited 19.8 ± 4.5% (1x load) and 76.5 ± 1.8% (2x load) increase in rise-times in comparison to the unloaded unbuffered system, and for the step-down experiment, the slow-down was 20.4 ± 1.7% (1x load) and 30.7 ± 2.7% (2x load) (Fig. 2A, Supplementary Fig 3). While the unbuffered system eventually reaches the same levels of expression regardless of load, the final output levels of the buffered system with low SKN7 and YPD1 expression are reduced due to load (Figs. 2B, Supplementary Figs. 3, 4). In contrast, the loaded buffered system with moderate SKN7 and YPD1 expression is unaffected by load, both in its temporal response and final output (Fig. 2C). Since the buffered system with moderate expression levels of SKN7 and YPD1 expression is able to attenuate retroactivity, we chose it for further evaluation. For this system, identical behavior is observed when the load module includes fluorescent reporters downstream of $P_{TR\text{-}SSRE}$ (Supplementary Fig. 5). Simulations performed with a detailed model of these biochemical processes correlate well with the theoretical analysis and experimental observations (Fig. 2 Insets, Supplementary Fig. 6). Note that while one might expect that addition of regulatory elements to a critical path of a system would slow down response times, here the converse was observed for the buffered versus unbuffered loaded systems.

We also examined the steady-state behavior of the systems. We performed step-up time-series experiments with intermediate DOX levels (Supplementary Fig. 7) and used these to generate the steady-state dosage-response of our systems. In agreement with our models, the load driver or load did not affect the final steady state (Fig. 2D). For the unbuffered system, the fact that the steady state does not change with addition of load is consistent with a system in which the interconnecting species (SKN7m) is protected from degradation when bound to DNA[17]. This is in contrast to other studies[27,28] where interconnecting species are not protected from degradation when bound to DNA and load may result in steady-state effects such as ultrasensitivity and thresholding. For the buffered system, the steady state does not change with the load provided that SKN7 amounts are sufficiently high (Fig. 2E and 2F). Our theoretical analysis shows that load driver steady-state dosage response is essentially linear, and determined by the ratio between the spontaneous rates of STAT5-HKRR phosphorylation and phospho-SKN7 dephosphorylation (Supplementary Note §1.5). The response curve slope is practically independent of any other parameter besides these two rates (Supplementary Note 1.6, Supplementary Fig. 8). Thus, when these two reaction rates are well balanced, the slope is approximately equal to one and hence the load driver does not affect the steady state.

To further characterize the load driver's ability to attenuate retroactivity, we next considered time-varying inputs. Specifically, we assayed system response to periodic square wave inputs. We used the simulation model in Fig. 2 to suggest input waveforms that display large retroactivity effects (Supplementary Note §1.3.3). Saturating DOX was initially applied followed by periodic square wave inductions with a fixed on-time of 50 minutes and varying periods (150, 200, 250, 350, and 500 minutes) to exponentially growing cultures. System trajectories were measured by flow cytometry (Fig. 3A, Supplementary Fig. 9) and this correlated well with simulations (Fig. 3B). For the waveforms analyzed, load on the unbuffered system resulted in an approximately 50 minute phase-lag, a 44% to 81% decrease in peak to peak amplitude of oscillations, and a 25% bandwidth reduction (Fig. 3C). By contrast, the buffered system exhibited almost no lag in the phase responses, minor amplitude deviations (4% to 12%), and negligible (0.5%) changes in bandwidth due to load (Fig. 3C).

In summary, load drivers can mitigate retroactivity when they operate at timescales much faster than those of the flanking modules and their QSS is independent of load. In our systems, the flanking modules are transcriptional networks with time scales in minutes to hours as determined by gene expression and protein decay[29]. Hence, molecular mechanisms with time scales in the seconds/sub-seconds are good candidates for a load driver, including phosphorylation, phosphotransfer, and methylation. To achieve the requirement of time scale separation, we chose to use a multi-stage phosphotranfer cascade (STAT5-HKRR to YPD1 to SKN7 phosphotransfer)[22,25] to implement our load driver. The amount of YPD1 and SKN7 used ensures the fast time scale essential for quickly approaching the QSS and negligible retroactivity effects on the QSS itself. In the current experimental setup, YPD1 and SKN7 levels are moderate and estimated to be at the 75th and 53th percentiles (6,325 and 2,572 protein copies per cell, respectively) of yeast protein expression levels[30]. For load drivers to handle increasing amounts of load at the same level of performance requires an approximately linear increase in the concentrations of YPD1 and SKN7, up to some limit

(Supplementary Fig. 10), which can be readily accomplished with stronger promoters. Furthermore, the load driver's output QSS should be an approximately linear function of the input. Criteria for obtaining this linear characteristic depend on the molecular mechanisms and have been extensively studied for covalent modification processes[46,47].We have chosen to implement the load driver using a two-stage phosphotransfer cascade, as opposed to (for example) a one-stage cascade. With one-stage cascades, the requirement that the QSS is independent of load is in conflict with the requirement of fast load driver dynamics[48], but this is not a limitation for systems with multiple stages, illustrated in detail in Supplementary Note §1.7.

To date the creation of synthetic gene networks has largely focused on engineering circuits that involve only slow processes, such as gene expression, or only fast processes, such as signal transduction. By contrast, in this manuscript we describe construction of a system based on a new design principle for engineering biological systems that combines slow and fast processes to mitigate loading effects in connected modules. We anticipate that in synthetic biology, load drivers will serve a role similar to that of unity-gain amplifying buffers in electronics. These buffers enable reliable and predictable connection of subsystems by eliminating load-induced alterations to the input-output characteristics of these subsystems[49]. In electronics, selective incorporation of amplifying buffers simplifies and dramatically speeds up the design process since circuits no longer require optimization or even re-design when new connections are formed. Analogously, we envision selective incorporation of multiple orthogonal load drivers into synthetic gene circuits will mitigate retroactivity arising from module interconnections (Box 2). Generation of load driver libraries and effective rules for incorporating load drivers into synthetic circuits will foster more predictable creation of complex systems.

Online Materials and Methods

Experimental

Reagents

Nucleic acid manipulation: AccuPrime Pfx SuperMix from Life Technologies and oligonucleotides manufactured by Integrated DNA Technologies were used for all PCR amplification. Oligonucleotides used in PCR are listed in Supplementary Table 1, used for sequencing are listed in Supplementary Table 2, and used to generate yeast knock-out are listed in Supplementary Table 3. BP Clonase II Enzyme Mix and LR Clonase II Plus Enzyme Mix from Life Technologies were used for all BP and LR reactions respectively (Supplementary Table 4). Taq ligase, NAD+, dNTPs, and Phusion Polymerase from New England Biolabs and T5 Exonucelase from Epicentre Biotechnologies were used for Gibson assembly reactions[31]. All other restriction enzymes obtained from New England Biolabs. All buffer components obtained from Sigma-Aldrich.

Bacteria: All plasmid construction utilized *E. coli* strain *E. cloni* 10G (Lucigen) made chemical competent by kit (Zymo Research) and were transformed by the suggested Z-comp heat-shock procedure. Bacterial cultures were grown in LB medium (BD Biosciences) and

supplemented with kanamycin, ampicillin, and chloramphenicol (Sigma-Aldrich) as appropriate.

Yeast: All strains are listed in Supplementary Table 6 and were prepared using standard transformation procedures[32]in a yeast strain with W303 background, YSC1058 (ThermoFisher Scientific). 5-Fluoroorotic Acid (5-FOA) was bought from Zymo Research, phleomycin from Invivogen, and G418 from Stratagene. All Synthetic Defined -URA (SD-URA) dropout media contained dextrose and was formulated by Sunrise Science. ssDNA was obtained from Life Technologies and all other chemical components from Sigma-Aldrich.

DNA circuit construction—The hierarchical assembly protocol outlined in Guye *et. al* was followed using yeast specific components[33].

Plasmid DNA constructs for promoter ENTR vectors: All relevant PCR primers are listed in Supplementary Table 1. All promoter ENTR vectors were verified by sequencing using standard M13F(−21) and M13R primers.

pENTR_L4-pTEF-R1 was prepared by PCR amplification of pTEF from pYM-N183[34] (EUROSCARF Accession No. P30274) using LD001, LD002, digesting the resulting fragment by XhoI, EcoRI and ligation using T4 DNA Ligase into a XhoI, EcoRI linearized pDONR-L4-R1 vector backbone.

pENTR_L4-pSSRE-R1 was prepared by PCR amplification of pSSRE from p413-SSRE-GFP [23] (Genbank DQ232595) using LD003, LD004, digesting the resulting fragment by XhoI, EcoRI and ligation using T4 DNA Ligase into a XhoI, EcoRI linearized pDONR-L4-R1 vector backbone.

pENTR_L4-pTR-SSRE-R1 was prepared by PCR amplification of pTR-SSRE from p413-TR-SSRE-GFP [23] (Genbank DQ232596) using LD003, LD004, digesting the resulting fragment by XhoI, EcoRI and ligation using T4 DNA Ligase into a XhoI, EcoRI linearized pDONR-L4-R1 vector backbone.

pENTR_L4-pTET-R1 was prepared by PCR amplification of pTET from pCM185 [35] (EUROSCARF Accession No. P30322) using LD 005, LD 006, digesting the resulting fragment by XhoI, EcoRI and ligation using T4 DNA Ligase into a XhoI, EcoRI linearized pDONR-L4-R1 vector backbone.

Plasmid DNA constructs for gene ENTR vectors: All PCR primers and sequencing primers are listed in Supplementary Table 1 and 2 respectively.

pENTR_L1-rtTA-L2 was prepared by PCR amplification of rtTA from pCM252[35] (EUROSCARF Accession No. P30340) using LD007, LD008 to produce flanking attB sites and a subsequent BP reaction utilizing pDONR221 (Life Technologies); sequenced using LDs001, LDs002.

pENTR_L1-SKN7-L2 was prepared by PCR amplification of SKN7 from isolated yeast genomic DNA using LD009, LD010 to produce flanking attB sites and a subsequent BP reaction utilizing pDONR221; sequenced using LDs003, LDs004.

pENTR_L1-SKN7m-L2 was prepared by site-directed mutagenesis on pENTR_L1-SKN7-L2 to produce SKN7 with D427E using the QuikChange Multi Site-Directed Mutagenesis Kit (Agilent); sequenced using LDs003, LDs004, LDs005.

pENTR_L1-JAK2-L2 was prepared by PCR amplification of JAK2 from mouse genomic DNA using LD011, LD012 to produce flanking attB sites and a subsequent BP reaction utilizing pDONR221; sequenced using standard M13F(−21) and M13R.

pENTR_L1-JH1-L2 was prepared by PCR amplification of JH1 from pENTR_L1-JAK2-L2 using LD013, LD014 to produce flanking attB sites and a subsequent BP reaction utilizing pDONR221; sequenced using LDs006, LDs007.

pENTR_L1-eGFP-L2 was prepared by PCR amplification of eGFP from p413-SSRE-GFP[23] (Genbank DQ232595) using LD015, LD016 to produce flanking attB sites and a subsequent BP reaction utilizing pDONR221; sequenced using LDs008, LDs009.

pENTR_L1-STAT5HKRR-L2 was prepared by PCR amplification of previously constructed STAT5-HKRR (gift from Ming-Tan Chen) using LD017, LD018 to produce flanking attB sites and a subsequent BP reaction utilizing pDONR221; sequenced using LDs010, LDs011, M13R.

pENTR_L1-kanMX-L2 was prepared by PCR amplification of kanMX from pYM-N183[34] (EUROSCARF Accession No. P30274) using LD019, LD020 to produce flanking attB sites and a subsequent BP reaction utilizing pDONR221; sequenced using LDs12, LDs13.

pENTR_L1-blank-L2 was prepared from a BP reaction between LD021 and pDONR221; sequenced using LDs14, LDs15.

pENTR_L1-YPD1-L2 was obtained from the Dana-Farber/Harvard Cancer Center Plasmid Repository (HIP Clone ID 201048); sequenced using M13(−21)F and M13R.

DNA constructs for unbuffered, buffered systems, and load—Destination vectors with position sequences flanking [attR4 – Gateway cassette – attR2 – yeast terminator] were used for all LR reactions. Supplementary Table 4 summarizes LR reactions performed using a low-volume modified Gateway reaction protocol[36]. All plasmids were sequence verified using corresponding oligos described earlier in ENTR vector construction in Supplementary Table 2.

Unbuffered/buffered circuits: Transcriptional units were combined using Gibson assembly into a PacI linearized carrier vector containing a [HO-L homology region – Seq1 – PacI – SeqX – HO-R homology region] cassette. The final circular plasmids were verified by sequencing using corresponding oligos described in Supplementary Table 2. The plasmids pLDUNB (unbuffered system), pLDBUFL (buffered system with low YPD1/SKN7), and

pLDBUF (buffered system) are listed in Supplementary Table 5. A cartoon representation of the plasmids pLDUNB (unbuffered system) and pLDBUF (buffered system) appear in Supplementary Figure 1.

Load plasmids: Similar to the unbuffered/buffered plasmids, transcriptional units were combined using Gibson assembly into a PacI linearized yeast-bacteria shuttle carrier vector based on pRS426 containing [Seq1 – PacI – SeqX]. The final circular plasmids were verified by sequencing using corresponding oligos described in Supplementary Table 2 and restriction mapping due to repetitive elements; a representation of the circular plasmids pLD00X (0X Load), pLD01X (1X Load), and pLD02X (2X Load) appear in Supplementary Figure 2 and are listed in Supplementary Table 5.

Yeast strains—In our experimental implementation of the load driver, we made several design choices. The device incorporates HK-RR phosphotransfer because this motif is well-characterized both mechanistically and structurally[37]. In the future, this may also allow several load drivers built from orthogonal HK-RR pairs to be implemented concurrently in a single cell[38]. In Dean[39], it is postulated that the domains of SLN1 can be separated out between the extracellular portions, the histidine kinase domain, and the first response regulator domain. Moreover, in Chen *et. al*[23], the HK-RR domains of SLN1 were successfully fused to AtCRE1 to form a fully functioning protein. Thus, the JH1-STAT5 interaction was favored over common bzip-type leucine zippers owing to the well characterized dimerization and protein structure and new fusion proteins were created. These proteins were tested in the context of DOX-inducible expression of the Jak2 protein or JH1 domain, galactose inducible expression of STAT5-HKRR, and the use of an integrated $P_{TR\text{-}SSRE}$ promoter. The data is presented in Broach *et. al*[40]. In this technical report, it is seen that there is positive signal transduction from input - JH1 - STAT5-HKRR - YPD1 - SKN7 - output.

To maintain specificity of YPD1 activation by STAT5-HKRR, we removed endogenous SLN1-YPD1 reactions by creation of a ΔSLN1 strain. Under normal growth conditions, coupling of SLN1-YPD1-SSK1/SKN7 to the HOG1 pathway renders the ΔSLN1 phenotype lethal[41]. Thus, we also created ΔHOT1 and ΔHOG1 knockouts to remove undesired upregulation of HOG1 resulting from the ΔSLN1 phenotype and hence rescue the lethal phenotype[42]. We chose to knock out HOG1 and HOT1 instead of further knocking out the high osmolarity pathway components SSK1 or SSK2 because ΔSSK1 would have exacerbated lethality and ΔSSK2 would not have guaranteed rescue due to SSK22 redundancy and/or PBS2 promiscuity leading to possible HOG1 activation. The deletion strain (ΔHOG1ΔHOT1ΔSLN1) growth characteristics were similar to wild-type strains under normal growth conditions (Supplementary Figure 11).

In the case of the buffered system with low YPD1 and SKN7, a second deletion strain was desired (YLD2) with the phenotype ΔHOG1ΔHOT1ΔSLN1ΔSKN7ΔYPD1. However, because the YPD1 deletion is a synthetic lethal, this strain was constructed by first knockout of SKN7 then subsequent integration of pLDBUFL into the HO locus and then knockout of YPD1 as described below. The promoter pair for SKN7/YPD1 expression were chosen from the literature to express at approximately 10–30% of the wildtype SKN7/YPD1 levels [30,43].

We integrated all exogenous transcriptional units as a single copy with kanMX selection into the growth-neutral HO locus[44] and did not observe experimentally any alterations to the growth characteristics (Supplementary Figure 11). To maintain promoter activity as our device output interface, the load must minimally consist of identical pTR-SSRE promoter sequences. These promoters were fused with downstream terminator sequences (Supplementary Fig. 2). All transformations utilized the standard LiAc protocol[32]. A list of all oligonucleotides used in gene disruption are in Supplementary Table 3 and a summary of all yeast strains appears in Supplementary Table 6.

A special multi-reporter load plasmid was constructed using the LR-Gibson assembly method described below with the first TR-SSRE promoter driving mCherry and the second TR-SSRE promoter driving Azurite. The experimental results are reported in Supplementary Figure 5.

Yeast strain with gene deletions: All knock-out strains were prepared by Cre-lox genetic disruption as previously described [45].

YLD (W303A in ΔHOG1ΔHOT1ΔSLN1 background)}

1. Intermediate W303 in ΔHOG1 background

   loxP flanked *K. lactis* URA3 was amplified by PCR from pUG72 [45] (EUROSCARF Accession No. P30117) using LDk001, LDk002 and then transformed into W303 yeast prior to selection. Clones were verified for successful integration by colony PCR before following standard transformation of the Cre containing plasmid, pSH65 [45] (EUROSCARF Accession No. P30122), followed by selection/counterselection protocols and colony PCR verification.

2. Intermediate W303 in ΔHOG1ΔHOT1 background

   loxP flanked *K. lactis* URA3 was amplified by PCR from pUG72 using LDk003, LDk004 and then that product was amplified further by LDk005, LDk006. This PCR fragment was transformed into the W303 strain with ΔHOG1 background described above. Subsequent steps proceeded as described in HOG1 deletion.

3. Final strain, YLD

   loxP flanked *K. lactis* URA3 was amplified from pUG72 using LDk007, LDk008. This PCR fragment was transformed into the W303 with ΔHOG1 ΔHOT1 background described above. Subsequent steps proceeded as described previously in HOG1 deletion.

YLD02 (W303 in ΔHOG1ΔHOT1ΔSLN1ΔSKN7ΔYPD1 background)

1. Intermediate W303A in ΔHOG1ΔHOT1ΔSLN1ΔSKN7}

   loxP flanked *K. lactis* URA3 was amplified by PCR from pUG72 using LDk009, LDk010. This PCR fragment was transformed into the YLD strain described above. Subsequent steps proceeded as described in HOG1 deletion.

2. Intermediate W303A in ΔHOG1ΔHOT1ΔSLN1ΔSKN7 with pLDBUFL}

Integration of pLDBUFL proceeded as decribed below.

3. Final Strain YLD02}

   loxP flanked *K. lactis* URA3 was amplified from pUG72 using LDk011, LDk012. This PCR fragment was transformed into the prior strain described above. Subsequent steps proceeded as described previously in HOG1 deletion.

The strains all had similar growth characteristics to wild-type (Supplementary Figure 11).

Yeast strains with integrated circuits and load: All circuit strains with load were prepared in the following manner. First, the unbuffered and buffered system plasmids (pLDUNB, pLDBUFL, pLDBUF) were linearized with I-SceI and purified by Qiagen PCR Cleanup Kit before subsequent LiAc transformation into strain YLD and selection on YPAD solid media supplemented with G418. Clones were verified for successful integration into the HO locus by colony PCR. Second, the unbuffered clone was transformed with a single pLD00X, pLD01X, or pLD02X plasmid and selected on YPAD media supplemented with URA and G418. This step was repeated for the buffered clone yielding a total of 9 strains YLDU00, YLDU01, YLDU02, YLDBL00, YLDBL01, YLDBL02, YLDB00, YLDB01, and YLDB02 with properties listed in Supplementary Table 6. These strains follow the naming convention, yeast load driver (YLD), followed by (U/B/BL) for integrated unbuffered or buffered/buffered low system, and ending with (00/01/02) corresponding to the amount of load.

Cell culture—Yeast strains harboring circuits and load, YLDU00, YLDU01, YLDU02, YLDB00, YLDB01, and YLDB02 were grown in SD –URA liquid media supplemented with G418 for 16 hours and combined with equal parts glycerol to form cell stocks. For all experiments, these cell stocks were used to inoculate 4mL liquid cultures and grown under full selection for 12 hours at 30C on a rotary shaker at 280rpm. These ‘starter cultures’ were diluted to OD660 = 0.10 and grown under selection for 2 additional hours at 30C with 280rpm rotary shaking before being collected by centrifugation and re-suspended in fresh selection media for experiments. OD660 was obtained using a NanoDrop 2000c (NanoDrop, Wilmington, DE) and calibrated to cell density counts via a haemocytometer calibration curve Supplementary Figure 11.

Step-up pertubation: Cultures at OD660 = 0.20 were grown under selection at 30C on rotary shaker at 280rpm in 4mL liquid cultures for 1060 minutes with aliquots removed every 20 minutes (t=0 – 300min) or every 40 minutes (t=300 – 1060min) for cytometry. 20μM DOX was added to liquid cultures at t=100 minutes and maintained for full 1060 minutes. OD660 was maintained between 0.20 and 0.60 via periodic dilution of cultures with fresh media containing appropriate inducer.

Step-down pertubation: Cultures at OD660 = 0.20 were grown under selection at 30C on rotary shaker at 280rpm in 4mL liquid cultures for 1000 minutes with 20μM DOX and periodic dilution with fresh media containing appropriate inducer to keep OD660 between 0.20 and 0.60. After 1000 minutes, cultures were diluted to OD660 = 0.2 with DOX at t = 0min and grown in 4mL liquid cultures with aliquots drawn at 50 and 100 minutes. At 100

minutes, cultures were centrifuged to remove DOX and grown under selection in 4mL liquid cultures for 1800 minutes with aliquots removed every 50 minutes for cytometry.OD660 was maintained between 0.20 and 0.60 via periodic dilution of cultures with fresh media.

Periodic injections: Cultures at OD660 = 0.20 were grown under selection at 30C on rotary shaker at 280rpm in 4mL liquid cultures for 1500 minutes with DOX introduction or removal by centrifugation and periodic dilution with fresh media to maintain OD660 between 0.20 and 0.60. Aliquots were removed every 50 minutes for cytometry. Initial induction times were as follows: 150min injection - 150min induction; 200min injection - 150min induction; 250min injection - 125min induction; 350min injection - 50min induction; 500min injection - 50min induction. Following these induction times, wave forms with 50 minutes DOX high and the remainder of the injection period DOX absent were applied.

Flow cytometry measurement: The same LSRFortessa flow analyzer (BD Biosciences) was used for all flow cytometry using the following sets of setting. eGFP was measured using a 488 nm laser, a 530/15 emission filter using a PMT of 360 V. For each sample, 30,000 events were collected and gated according to FSC-A (PMT of 130V) and SSC-A (PMT of 100V). In parallel, Rainbow Calibration Particles (Spherotech RCP-30-5A) were measured to equalize data between different experimental runs (see Data Analysis).

Data analysis

Flow cytometry: Line plots in Figs. 2, Supplementary Figures 4 and 5 were generated as follows. For each sample, the corresponding reference standard calibration was defined using FlowJo (TreeStar Software) to obtain a new channel, FITC-Calibrated. Next, the median value of FITC-Calibrated was calculated for each sample. Those median values were then graphed (or the mean of replicate medians in the case of Fig. 2) utilizing Prism (GraphPad Software). Adjacent points are connected by straight lines.

Rise and decay times: Rise-times for a step-up input in Fig. 2 were calculated for only the unbuffered and moderate buffered system as follows. Eighteen individual datasets (3 replicates of unbuffered–0x, unbuffered–1x, unbuffered–2x, moderate buffered–0x, moderate buffered–1x, moderate buffered–2x) were loaded into MATLAB (The Mathworks, Natick, MA). For each individual trajectory, a minimum value, the average of the first 3 data points ($t \leq 0$min) for each single trajectory was calculated. The minimum value was subtracted from every data point of its corresponding trajectory to eliminate bias i.e. the data range was shifted to start at zero rather than the approximately 300 A.U. from the instrument. For the 3 unbuffered–0x trajectories and 3 buffered–0x trajectories, a maximum value, the average of the last 3 data points of each single trajectory, was calculated. These individual 0x trajectories were averaged to yield $\text{UnbufferedMax}_{\text{Mean}}$ and $\text{BufferedMax}_{\text{Mean}}$. All 9 unbuffered trajectories were normalized by dividing each data point by $\text{UnbufferedMax}_{\text{Mean}}$ and all 9 buffered trajectories were normalized by dividing each data point by $\text{BufferedMax}_{\text{Mean}}$. This normalization allows accurate comparison between loaded systems and the control, unloaded system. For each unbuffered trajectory, linear piece-wise interpolation was performed to obtain the response time, the time necessary to

reach 90% of $\text{UnbufferedMax}_{\text{Mean}}$. This was repeated for buffered trajectories using $\text{BufferedMax}_{\text{Mean}}$. The interpolated rise-times were averaged and the means and standard deviation are as follows: Unbuffered: 0x Load – 396.1 ± 23.0 min; 1x Load – 474.6 ± 45.3 min; 2x Load – 698.9 ± 47.9 min; Buffered: 0x Load – 432.4 ± 8.9 min; 1x Load – 420.2 ± 20.9min; 2x Load – 423.2 ± 21.5 min. To calculate the slow-down to reach 90% maximum value as reported in the main text, the following formula was employed:

$$100\% \cdot \frac{Loaded_{Mean} - Unloaded_{Mean}}{Unloaded_{Mean}}$$

Error in percentages follows the standard propagation of uncertainty using the partial derivative rule and is obtained from:

$$100\% \cdot \left| \frac{Loaded_{Mean}}{Unloaded^2_{Mean}} \cdot Unloaded_{SD} - \frac{Loaded_{SD}}{Unloaded_{Mean}} \right|$$

Decay-times for a step-down input in Fig. 2 were calculated similarly to rise-time for only the unbuffered and moderate buffered system as follows with several deviations. For each individual trajectory, a minimum value, the average of the last 3 data points for each single trajectory was calculated. This minimum value was subtracted from every data points of its corresponding trajectory to eliminate bias i.e. the data range was shifted to start at zero rather than the approximately 300 A.U. from the instrument. For the 3 unbuffered–0x trajectories and 3 buffered–0x trajectories, a maximum value, the average of the last 3 data points ($t \leq 0$ min) of each single trajectory, was calculated. These individual 0x trajectories were averaged to yield $\text{UnbufferedMax}_{\text{Mean}}$ and $\text{BufferedMax}_{\text{Mean}}$. The trajectories were normalized to their corresponding average. For each unbuffered trajectory, linear piece-wise interpolation was performed to obtain the response time, the time necessary to reach 10% of $\text{UnbufferedMax}_{\text{Mean}}$. This was repeated for buffered trajectories using $\text{BufferedMax}_{\text{Mean}}$. The interpolated decay-times were averaged and the means and standard deviation are as follows: Unbuffered: 0x Load – 1044.1 ± 31.2min; 1x Load –1256.6 ± 19.4min; 2x Load – 1364.6 ± 12.9 min; Buffered: 0x Load –1024.4 ± 36 min; 1x Load –1021.9 ± 38.5 min; 2x Load –1043.6 ± 23.6 min. To calculate the slow-down to reach 10% maximum value as reported in the main text, the means and deviations were used in the same formulas as above.

The slow-down for the unbuffered systems are reported in the main text. For the buffered system with moderate SKN7 and YPD1 expression, their values are reported here. The step-up response exhibited a 2.83 ± 2.84% (1x load) and 2.13 ± 2.94% (2x load) change in rise-time compared to the unloaded buffered system and for the step-down experiment, the system had −0.24 ± 0.25% (1x load) and 1.88 ± 1.27% (2x load) change in decay-times

Amplitude attenuation: Amplitudes in Fig. 3B were calculated as follows. The datasets were loaded into MATLAB and the local minimum and local maximum values of trajectories starting at the injection point until the next injection point were found. The corresponding values were subtracted such that a peak-to-peak amplitude was obtained.

Averages and SD plotted were obtained using the last three injections of each 1500min experiment. System amplitude differences expressed as relative error between loaded and unloaded are as follows: Unbuffered: 150min – 44.1 ± 25.8%; 200min – 80.8 ± 3.8%; 250min – 61.8 ± 0.9%; 350min – 49.2 ± 2.0%; 500min – 57.6 ± 2.2%. Buffered: 150min – 5.9 ± 10.7%; 200min – 7.6 ± 25.6%; 250min – 12.2 ± 5.3%; 350min – 4.0 ± 4.5%; 500min – 5.2 ± 3.7%.

Mathematical

We include a supplemental note that within it contains several sections providing mathematical and computational methods and analysis in support of the load driver. Supplementary Note §1.1 describes use of time scale separation for retroactivity attenuation. Supplementary Note §1.2 contains the mathematical derivations necessary for Box 1. Supplementary Note §1.3 – 1.6 provides a comprehensive description of the formulation, assumptions, parameters, and analysis of mathematical models for the unbuffered and buffered circuits shown in Fig. 1. Supplementary Note §1.7 – 1.8 includes mathematical analysis and results of load drivers built with one to two stages as well as the use of load drivers and load encoded on medium copy plasmids instead of high copy or integrated circuits are used.

Unbuffered and Buffered Models Summary—We formulated mathematical models for the unbuffered and buffered circuits shown in Fig. 1. We utilized these models to both assess the effect of retroactivity in the specific circuit implementations chosen for the experiments and to demonstrate that the chosen load driver circuit implementation of Fig. 1E satisfies the structure and assumptions required for retroactivity attenuation illustrated in Supplementary Note §1.1. Each system was written as a set of reactions governing protein species and then using mass action kinetics, formed into a set of Ordinary Differential Equations (ODEs). These ODEs were then used to construct a grey-box model using the MATLAB System ID Toolbox (The Mathworks). Experimental datasets were used to fit parameters of the grey-box model using the Trust-Region-Reflective Least Squares algorithm. Final simulations were performed using a stiff differential equation solver (MATLAB ode23s) and final parameter values listed in Supplementary Table 7. A comprehensive description of the model is included in the supplemental note. A mapping from the mathematical model used to the schematics from the main text appears in Supplementary Note §1.3. Additionally, the code is available online as supplementary material.

Supplementary Material

Refer to Web version on PubMed Central for supplementary material.

Acknowledgments

We thank members of the Weiss and Del Vecchio labs for discussions; M-T Chen for plasmids containing STAT5-HKRR and JAK2, and the Synthetic Biology Center at MIT's cytometry facility. D.M. was supported by the Eni-MIT Energy Research Fellowship and both D.M. and P.M.R. were supported by NSF GRFP under Grant DGE-1122374. This research was supported by the NSF (CCF-1058127), NSF SynBERC (SA5284-11210), USAFOSR (FA9550-12-1-0129), USARO ICB (W911NF-09-D-0001), and the NIH (P50 GM098792).

References

1. Cardinale S, Arkin AP. Contextualizing context for synthetic biology--identifying causes of failure of synthetic biological systems. Biotechnol. J. 2012; 7:856–866. [PubMed: 22649052]
2. Purnick PEM, Weiss R. The second wave of synthetic biology: from modules to systems. Nat. Rev. Mol. Cell Biol. 2009; 10:410–422. [PubMed: 19461664]
3. Hartwell LH, Hopfield JJ, Leibler S, Murray AW. From molecular to modular cell biology. Nature. 1999; 402:C47–C52. [PubMed: 10591225]
4. Lauffenburger DA. Cell signaling pathways as control modules: complexity for simplicity? Proc. Natl. Acad. Sci. U. S. A. 2000; 97:5031–5033. [PubMed: 10805765]
5. Del Vecchio D, Ninfa AJ, Sontag ED. Modular cell biology: retroactivity and insulation. Mol. Syst. Biol. 2008; 4:161. [PubMed: 18277378]
6. Lou C, Stanton B, Chen Y-J, Munsky B, Voigt CA. Ribozyme-based insulator parts buffer synthetic circuits from genetic context. Nat. Biotechnol. 2012; 30:1137–1142. [PubMed: 23034349]
7. Qi L, Haurwitz RE, Shao W, Doudna JA, Arkin AP. RNA processing enables predictable programming of gene expression. Nat. Biotechnol. 2012; 30:1002–1006. [PubMed: 22983090]
8. Bashor CJ, Collins JJ. Insulating gene circuits from context by RNA processing. Nat. Biotechnol. 2012; 30:1061–1062. [PubMed: 23138300]
9. Ellis T, Wang X, Collins JJ. Diversity-based, model-guided construction of synthetic gene networks with predicted functions. Nat. Biotechnol. 2009; 27:465–471. [PubMed: 19377462]
10. Atkinson MR, Savageau MA, Myers JT, Ninfa AJ. Development of genetic circuitry exhibiting toggle switch or oscillatory behavior in Escherichia coli. Cell. 2003; 113:597–607. [PubMed: 12787501]
11. Elowitz MB, Leibler S. A synthetic oscillatory network of transcriptional regulators. Nature. 2000; 403:335–338. [PubMed: 10659856]
12. Gardner TS, Cantor CR, Collins JJ. Construction of a genetic toggle switch in Escherichia coli. Nature. 2000; 403:339–342. [PubMed: 10659857]
13. Hooshangi S, Thiberge S, Weiss R. Ultrasensitivity and noise propagation in a synthetic transcriptional cascade. Proc. Natl. Acad. Sci. U. S. A. 2005; 102:3581–3586. [PubMed: 15738412]
14. Endy D. Foundations for engineering biology. Nature. 2005; 438:449–4453. [PubMed: 16306983]
15. Kim Y, et al. Substrate-dependent control of MAPK phosphorylation in vivo. Mol. Syst. Biol. 2011; 7:467. [PubMed: 21283143]
16. Jiang P, et al. Load-induced modulation of signal transduction networks. Sci. Signal. 2011; 4:ra67. [PubMed: 21990429]
17. Jayanthi S, Nilgiriwala KS, Del Vecchio D. Retroactivity controls the temporal dynamics of gene transcription. ACS Synth. Biol. 2013; 2:431–441. [PubMed: 23654274]
18. Brewster RC, et al. The transcription factor titration effect dictates level of gene expression. Cell. 2014; 156:1312–1323. [PubMed: 24612990]
19. Ventura AC, et al. Signaling properties of a covalent modification cycle are altered by a downstream target. Proc. Natl. Acad. Sci. U. S. A. 2010; 107:10032–10037. [PubMed: 20479260]
20. Kim Y, et al. Gene regulation by MAPK substrate competition. Dev. Cell. 2011; 20:880–887. [PubMed: 21664584]
21. Jayanthi S, Del Vecchio D. Retroactivity attenuation in bio-molecular systems based on timescale separation. IEEE Trans. Automat. Contr. 2011; 56:748–761.
22. Lenssen E, Azzouz N, Michel A, Landrieux E, Collart Ma. The Ccr4-not complex regulates Skn7 through Srb10 kinase. Eukaryot. Cell. 2007; 6:2251–2259. [PubMed: 17965252]
23. Chen M-T, Weiss R. Artificial cell-cell communication in yeast Saccharomyces cerevisiae using signaling elements from Arabidopsis thaliana. Nat. Biotechnol. 2005; 23:1551–1555. [PubMed: 16299520]
24. Futcher AB, Cox BS. Copy number and the stability of 2-micron circle-based artificial plasmids of Saccharomyces cerevisiae. J. Bacteriol. 1984; 157:283–290. [PubMed: 6361000]

25. Aaronson DS, Horvath CM. A road map for those who don't know JAK-STAT. Science (80−.). 2002; 296:1653–1655.
26. Janiak-Spens F, Cook PF, West AH. Kinetic analysis of YPD1-dependent phosphotransfer reactions in the yeast osmoregulatory phosphorelay system. Biochemistry. 2005; 44:377–386. [PubMed: 15628880]
27. Lee T-H, Maheshri N. A regulatory role for repeated decoy transcription factor binding sites in target gene expression. Mol. Syst. Biol. 2012; 8:576. [PubMed: 22453733]
28. Buchler NE, Cross FR. Protein sequestration generates a flexible ultrasensitive response in a genetic network. Mol. Syst. Biol. 2009; 5:272. [PubMed: 19455136]
29. Alon, U. An Introduction to Systems Biology: Design Principles of Biological Circuits. Chapman & Hall/CRC: 2013.
30. Ghaemmaghami S, et al. Global analysis of protein expression in yeast. Nature. 2003; 425:737–741. [PubMed: 14562106]
31. Gibson DG, et al. Enzymatic assembly of DNA molecules up to several hundred kilobases. Nat. Methods. 2009; 6:343–345. [PubMed: 19363495]
32. Gietz D, St Jean A, Woods RA, Schiestl RH. Improved method for high efficiency transformation of intact yeast cells. Nucleic Acids Res. 1992; 20:1425. [PubMed: 1561104]
33. Guye P, Li Y, Wroblewska L, Duportet X, Weiss R. Rapid, modular and reliable construction of complex mammalian gene circuits. Nucleic Acids Res. 2013
34. Janke C, et al. A versatile toolbox for PCR-based tagging of yeast genes: new fluorescent proteins, more markers and promoter substitution cassettes. Yeast. 2004; 21:947–962. [PubMed: 15334558]
35. Garí E, Piedrafita L, Aldea M, Herrero E. A set of vectors with a tetracycline-regulatable promoter system for modulated gene expression in Saccharomyces cerevisiae. Yeast. 1997; 13:837–848. [PubMed: 9234672]
36. Alberti S, Gitler AD, Lindquist S. A suite of Gateway cloning vectors for high-throughput genetic analysis in Saccharomyces cerevisiae. Yeast. 2007; 24:913–919. [PubMed: 17583893]
37. Laub MT, Goulian M. Specificity in two-component signal transduction pathways. Annu. Rev. Genet. 2007; 41:121–145. [PubMed: 18076326]
38. Whitaker WR, Davis Sa, Arkin AP, Dueber JE. Engineering robust control of two-component system phosphotransfer using modular scaffolds. Proc. Natl. Acad. Sci. U. S. A. 2012; 109:18090–18095. [PubMed: 23071327]
39. Dean S. Achieving specificity in yeast stress responses. 2004
40. Broach J. Highly extensible programmed biosensing curcuits with fast memory. 2011:1–26.
41. Ota IM, Varshavsky A. A yeast protein similar to bacterial two-component regulators. Science (80−.). 1993; 262:566–569.
42. Escoté X, Zapater M, Clotet J, Posas F. Hog1 mediates cell-cycle arrest in G1 phase by the dual targeting of Sic1. Nat. Cell Biol. 2004; 6:997–1002. [PubMed: 15448699]
43. Lee ME, Aswani A, Han AS, Tomlin CJ, Dueber JE. Expression-level optimization of a multi-enzyme pathway in the absence of a high-throughput assay. Nucleic Acids Res. 2013; 41:10668–10678. [PubMed: 24038353]
44. Voth WP, Richards JD, Shaw JM, Stillman DJ. Yeast vectors for integration at the HO locus. Nucleic Acids Res. 2001; 29:E59–E59. [PubMed: 11410682]
45. Gueldener U, Heinisch J, Koehler GJ, Voss D, Hegemann JH. A second set of loxP marker cassettes for Cre-mediated multiple gene knockouts in budding yeast. Nucleic Acids Res. 2002; 30:e23. [PubMed: 11884642]
46. Goldbeter A, Koshland D. An amplified sensitivity arising from covalent modification in biological systems. Proceedings of the National. 1981; 78:6840–6844.
47. Del Vecchio, D.; Murray, R. Biomolecular Feedback Systems. 1st edn. Princeton, NJ: Princeton University Press; 2014.
48. Rivera PM, Del Vecchio D. Optimal Design of Phosphorylation-Based Insulation Devices. Proceedings of the American Control Conference. 2013:3783–3789.
49. Millman, J.; Grabel, A. Microelectronics. 1st edn. New York: McGraw-Hill; 1987.

50. Franklin, G.; Powell, J.; Emami-Naeini, A. Feedback Control of Dynamic Systems. 6th edn. Upper Saddle River, NJ: Pearson; 2010.

51. Gyorgy A, Del Vecchio D. Modular composition of gene transcription networks. PLoS computational biology. 2014; 10:e1003486. [PubMed: 24626132]

52. Laub MT, Goulian M. Specificity in two-component signal transduction pathways. Annual review of genetics. 2007; 41:121–145.

53. Whitaker WR, Davis Sa, Arkin AP, Dueber JE. Engineering robust control of two-component system phosphotransfer using modular scaffolds. Proceedings of the National Academy of Sciences of the United States of America. 2012; 109:18090–18095. [PubMed: 23071327]

54. Perraud AL, Weiss V, Gross R. Signalling pathways in two-component phosphorelay systems. Trends in microbiology. 1999; 7:115–120. [PubMed: 10203840]

55. Workentine ML, Chang L, Ceri H, Turner RJ. The GacS-GacA two-component regulatory system of Pseudomonas fluorescens: a bacterial two-hybrid analysis. FEMS microbiology letters. 2009; 292:50–56. [PubMed: 19191877]

56. Schaller GE, Kieber JJ, Shiu S-H. Two-component signaling elements and histidyl-aspartyl phosphorelays. The Arabidopsis book / American Society of Plant Biologists. 2008; 6:e0112. [PubMed: 22303237]

57. Ansaldi M, Jourlin-Castelli C, Lepelletier M, Théraulaz L, Méjean V. Rapid dephosphorylation of the TorR response regulator by the TorS unorthodox sensor in Escherichia coli. Journal of bacteriology. 2001; 183:2691–2695. [PubMed: 11274133]

58. Reiser V, Raitt DC, Saito H. Yeast osmosensor Sln1 and plant cytokinin receptor Cre1 respond to changes in turgor pressure. The Journal of cell biology. 2003; 161:1035–1040. [PubMed: 12821642]

BOX 1: Time scale separation for retroactivity attenuation

Here we provide a simplified mathematical explanation of how retroactivity can be attenuated by a load driver that utilizes processes with time scales that are much faster than those of its flanking modules. A more in-depth and general mathematical analysis appears in Supplementary Note §1.2. Consider the block diagram in Fig. 1B, in which proteins create functional connections from the load driver to the upstream and downstream transcriptional systems. We define $u(t)$ as the load driver's time varying input protein concentration, y as the concentration of the load driver's output protein in its free active form, and c as the concentration of load driver's output protein bound to DNA binding sites in the downstream system.

To illustrate how time scale separation results in attenuation of retroactivity, we consider a basic model of the isolated load driver encoding processes that generate and remove the output protein y. We define the lumped parameter G to scale together the rates of production and removal of y yielding $G\,(u(t) - y)$. Here, larger values of G correspond to faster time scales of load driver dynamics. Upon interconnection with load, other reactions that affect y include reversible binding to downstream DNA sites in concentration p with the rate $k_{on}\,p\,y - k_{off}\,c$, in which k_{on} and k_{off} are "on" and "off" binding rate constants. The resulting system dynamics can be represented by two differential equations:

$$\frac{dy}{dt} = G \cdot (u(t) - y) - k_{on} \cdot p \cdot y + k_{off} \cdot c \quad \frac{dc}{dt} = k_{on} \cdot p \cdot y - k_{off} \cdot c. \qquad (1)$$

The reversible binding reactions between the load driver's active output protein and downstream DNA binding sites constitute retroactivity r, that is $r = k_{on}\,p\,y - k_{off}\,c$, and is shown in red. We refer to the system with $r = 0$ as the unloaded system and to the system where r is non-zero as the loaded system. We seek to understand how the time dependent response of y to $u(t)$ is affected by retroactivity when the time scale of the load driver dynamics becomes faster (G increases) in comparison to the speed of the input. To this end, consider a particular example where $u(t)$ is a periodic input (Box Fig. 1A). The simulation in Box Fig. 1B shows the system response to this input in the loaded (red) or unloaded (black) systems when the load driver operates at a slow timescale (low G). At slow timescales, the loaded system is unable to respond to the input signal effectively. In comparison, Box Fig. 1C shows a simulation for the same periodic input $u(t)$ with a load driver operating at a fast timescale (high G) where the effect of retroactivity is attenuated.

To understand this phenomenon, it is useful to graph the ratio between the oscillatory amplitudes of the output and the input as a function of the input frequency ω, that is, the magnitude M of the system's frequency response gain[50]. This is a common way to determine how a system responds to its input when the relative time scales change. Box Fig. 1D shows M as a function of the input frequency ω for the systems with low G (Box Fig. 1B). Box Fig. 1E shows the corresponding relationship for the systems with high G (Box Fig. 1C).

As derived in Supplementary Note §1.2,

$$M(\omega)=\frac{\alpha \cdot G}{\sqrt{\omega^2+(\alpha \cdot G)^2}},$$

in which α = 1 for the unloaded system and $\alpha=\left(1+\frac{p}{K_d}\right)^{-1}$ for the loaded system, where $k_d = k_{off}/k_{on}$ is the dissociation constant of the binding reaction. The cut-off frequency (also called bandwidth) is a convenient metric for quantifying the speed of a system and is defined as the frequency of the input such that the magnitude *M* drops below $1/\sqrt{2}$[48]. It can be found by solving the equation $M(\omega)=1/\sqrt{2}$ for ω, and for system (1) is equal to α *G*. Hence, when ω << α *G*, that is, the rate of change of the input is much slower than the dynamics of the load driver (shaded areas in Box Fig. 1D, 1E), we have that *M*(ω) ≈ 1. This implies that *y(t)* ≈ *u(t)*, which also corresponds to the quasi-steady state (QSS) value of the output obtained by viewing *u(t)* as a constant input in system (1) and by solving for the steady state. In this case, the output *y* is able to effectively follow *u(t)* independent of retroactivity. As retroactivity reduces the cut-off frequency since α < 1 (compare black and red plots in Box Fig 1D), an increase in *G* for the load driver extends the range of input frequencies where retroactivity is attenuated, i.e., where *M*(ω) ≈ 1 (compare red plots in Box Figs. 1D and 1E). Considering the input signal *u(t)* given in Box Fig. 1A, the magnitude of the frequency response gain of the unloaded and loaded systems corresponding to this specific input are marked by + and × respectively within Box Figs. 1D and 1E. When the separation of timescale between the load driver's dynamics and the input is increased, i.e., *G* is increased, the difference in *M* is eliminated and thus retroactivity is attenuated.

BOX 2: Inserting load drivers into more complex circuits

We describe a general process for inserting load drivers into complex multi-module networks to systematically mitigate retroactivity (Box 2 Fig. 1). Initially, a circuit is devised to solve a particular biological problem. The circuit is typically encoded as a set of interacting modules. Particular connections between all connected module pairs are examined one at a time for instance, upstream to downstream. For any connected pair, mathematical modeling is first used to predict the extent of retroactivity[51]. In cases where retroactive effects are unlikely, one can move on to the next connection.

In the event that retroactive effects are likely (based on modeling) upon the interconnection of two modules, the relevant sub-circuit is built and examined experimentally, to evaluate whether retroactivity predicted by modeling occurs *in vivo*. A suitable load driver is chosen. This load driver must be orthogonal to other load drivers that are already incorporated in the whole circuit. Furthermore, the load driver chosen must have the appropriate operational range and threshold matching, that is, the output of an upstream module must be within the input range of the load driver as well as the output of the load driver must be within the input range of the downstream module.

To load driver must operate on a faster time-scale than the modules in the circuit and thus, for transcriptional networks, should utilize molecular mechanisms faster than transcription such as phosphotransfer, methylation, or phosphorylation. Some multi-stage phosphotransfer pathways available for incorporation as load drivers are listed in Box 2, Table 1 or available two-component signaling motifs could be adapted[52]. Multiple phosphotransfer motifs can be concurrently implemented in a synthetic circuit within the same cell with adequate orthogonality[53] suggesting that load drivers of this form could be used simultaneously. For other regulatory modalities that operate at similar timescales to transcription (e.g., translational inhibition by RNA-binding proteins) and exhibit retroactivity, the load driver could still be based on phosphotransfer reactions. As regulatory modalities approach the timescales of the fastest known intracellular biochemical interactions, different approaches will need to be investigated for mitigation of load (e.g., effectively slowing down the flanking modules).

The load driver is inserted into the circuit and both modeling and experimentally validation are then required to show that retroactivity is mitigated for that connection. In the event that retroactive effects still exist, the load driver can be optimized by changing individual concentration of the load driver's proteins to handle larger amounts of load while enabling unity gain. In some cases, a particular load driver may be unable to be optimized to simultaneously achieve retroactivity attenuation and unity gain. This failure mode can be overcome by choosing a different load driver. Once loading effects are eliminated by inclusion of a load driver, the multi-module circuit topology can be updated and the next module interconnection can be examined for retroactive effects. When all module connections have been examined and load drivers incorporated appropriately, the process is complete.

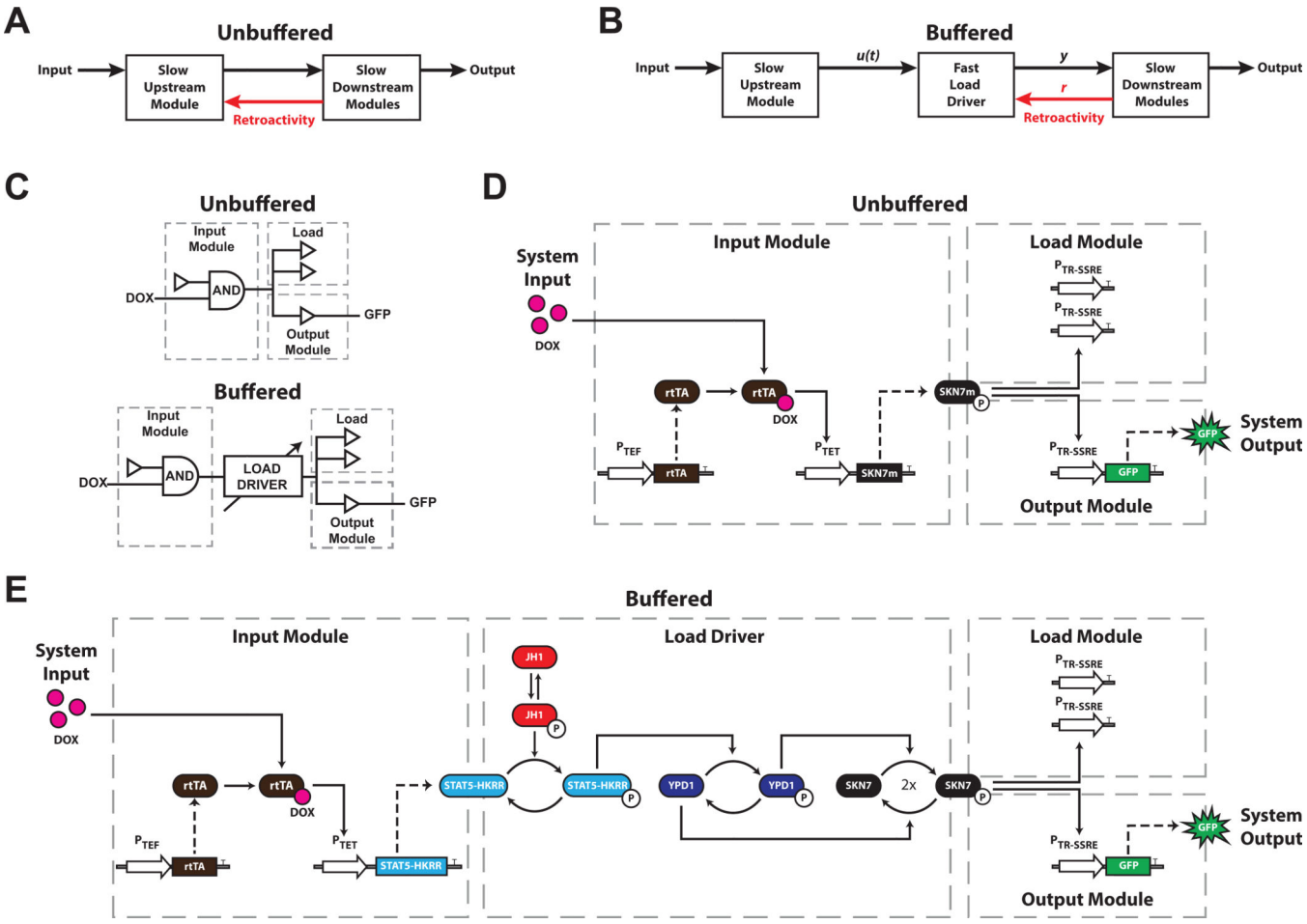

Fig. 1. Block diagrams of unbuffered and buffered systems

(A) Block diagram of a 2-module unbuffered system where an upstream module is connected directly to a downstream module. The downstream module applies retroactivity (red arrow) on the upstream module. **(B)** Creation of a buffered system via incorporation of an intervening fast load driver into the unbuffered system. Here, $u(t)$ is the input to the load driver, y is the output of the load driver, and r is the retroactivity. Retroactivity is transferred to the load driver (red arrow) while the load driver itself exerts negligible load on the upstream module. **(C)** Logic circuit representation of the experimental systems with variants that either include or do not include the load. All systems have DOX as input, GFP as output, and the same form of input and output modules. **(D)** Genetic implementation of the unbuffered system. DOX induction produces SKN7m that binds $P_{TR\text{-}SSRE}$, resulting in GFP expression. **(E)** Genetic implementation of the buffered system. DOX induction produces STAT5-HKRR. STAT5-HKRR is phosphorylated by JH1 and activates YPD1 by phosphotransfer. Two YPD1 proteins doubly activate SKN7[25] which then binds $P_{TR\text{-}SSRE}$, producing GFP. With respect to Fig. 1B and the analysis in Box 1, $u(t)$ represents the time-dependent concentration of STAT5-HKRR, y represents the concentration of phospho-SKN7, p represents the concentration of $P_{TR\text{-}SSRE}$ promoter sites, and c represents the concentration of $P_{TR\text{-}SSRE}$ bound phospho-SKN7. For Panels D and E, all promoters exist in single-copy on the chromosome except for the load TR-SSRE promoters which are on high-

copy 2μ plasmids. Experiments are performed in *S. cerevisiae* strain with *hot1*Δ*hog1*Δ*sln1*Δ background (see methods).

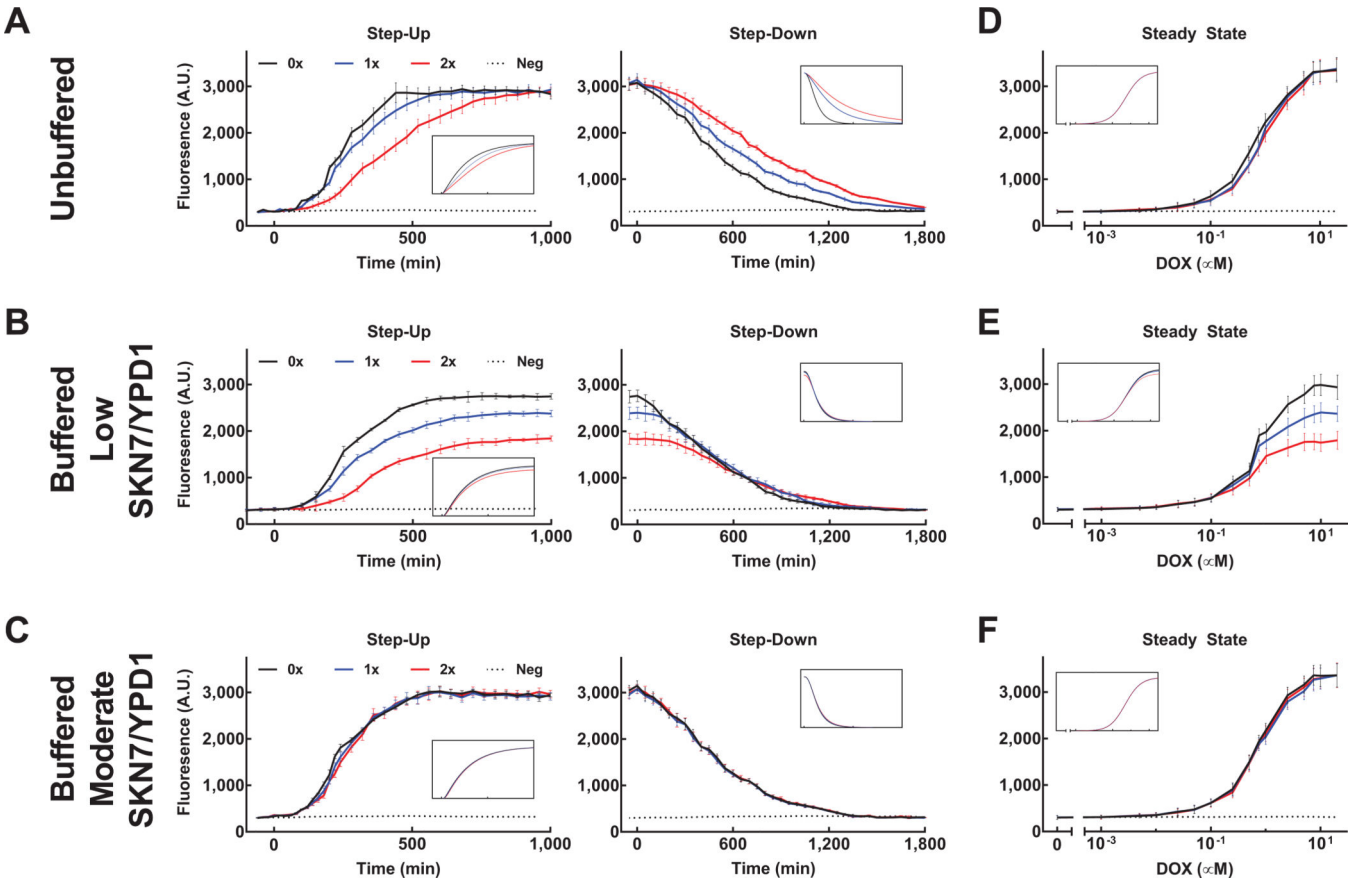

Fig. 2. System responses to step inputs and dosage-response

S. cerevisiae cells integrated with unbuffered (top), buffered system with low expression of SKN7 and YPD1 (middle), and buffered system with moderate expression of SKN7 and YPD1 (bottom) with 0x (black), 1x (blue), or 2x (red) load plasmids were grown in liquid culture (OD_{660} maintained at 0.2 – 0.6 via periodic dilution). Negative control for each panel is unloaded system that did not receive DOX. Error bars indicate standard deviation for n = 3 biological replicates. Insets of each panel show corresponding simulation results using parameters listed in Supplementary Table 7. **(A)** Unbuffered system response. Left panel is GFP response for cultures induced with 20μM DOX at t = 0 min. Right panel is GFP response for cultures previously induced with 20μM DOX and then removed at t = 0 min. **(B)** Buffered system with low SKN7 and YPD1 expression response. Panels are GFP response of this circuit for conditions outlined in panel A. **(C)** Response of buffered system with moderate SKN7 and YPD1 expression. Panels are GFP response of this circuit for conditions outlined in panel A. **(D)** Steady state response curves for unbuffered systems. Panel is GFP dosage-response across DOX concentrations for cultures measured at t = 1000 min post-induction. **(E–F)** Steady state response of buffered systems with low SKN7 and YPD1 expression (E) and moderate SKN7 and YPD1 expression (F). Panels are GFP dosage responses across DOX for same conditions as outlined in panel D.

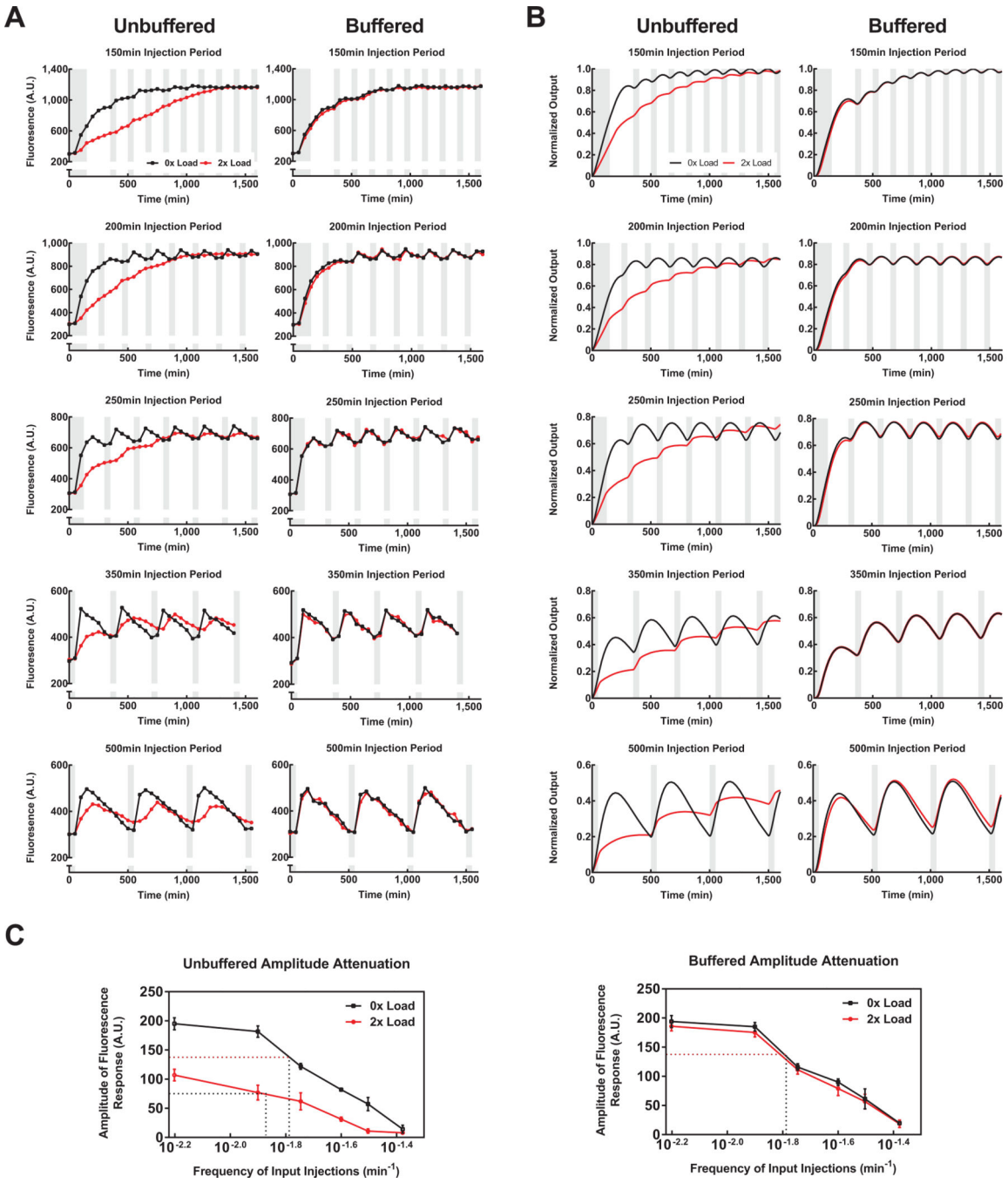

Fig. 3. System responses to periodic inputs

S. cerevisiae cells integrated with circuits with 0x (black) or 2x (red) load plasmids and grown in liquid culture (OD_{660} maintained at 0.2 – 0.6 via periodic dilution). Grey shading indicates application of 20μM DOX. Error bars in C indicate standard deviation for n = 3 oscillations of an individual trajectory. (**A)** Experimental GFP response trajectories from single cultures for unbuffered (left) and buffered (right) circuits when periodically induced by 20μM DOX followed by removal after 50 minutes. Injection time corresponds to time between successive DOX inductions. (**B)** Simulated GFP trajectories from a mathematical

model using parameter set fitted to full data sets with periodic DOX induction as described in panel A. Parameters used for simulations are given in Supplementary Table 8. (**C)** Amplitude of response for unbuffered systems (left) and buffered systems (right) across injection frequencies. Dotted lines correspond to calculated bandwidths and for the unbuffered system is 0.0140 min^{-1} and 0.0175 min^{-1} for the unloaded and loaded cases, respectively. The buffered system has bandwidths of 0.0142 min^{-1} and 0.0143 mn^{-1} for unloaded and loaded cases, respectively.

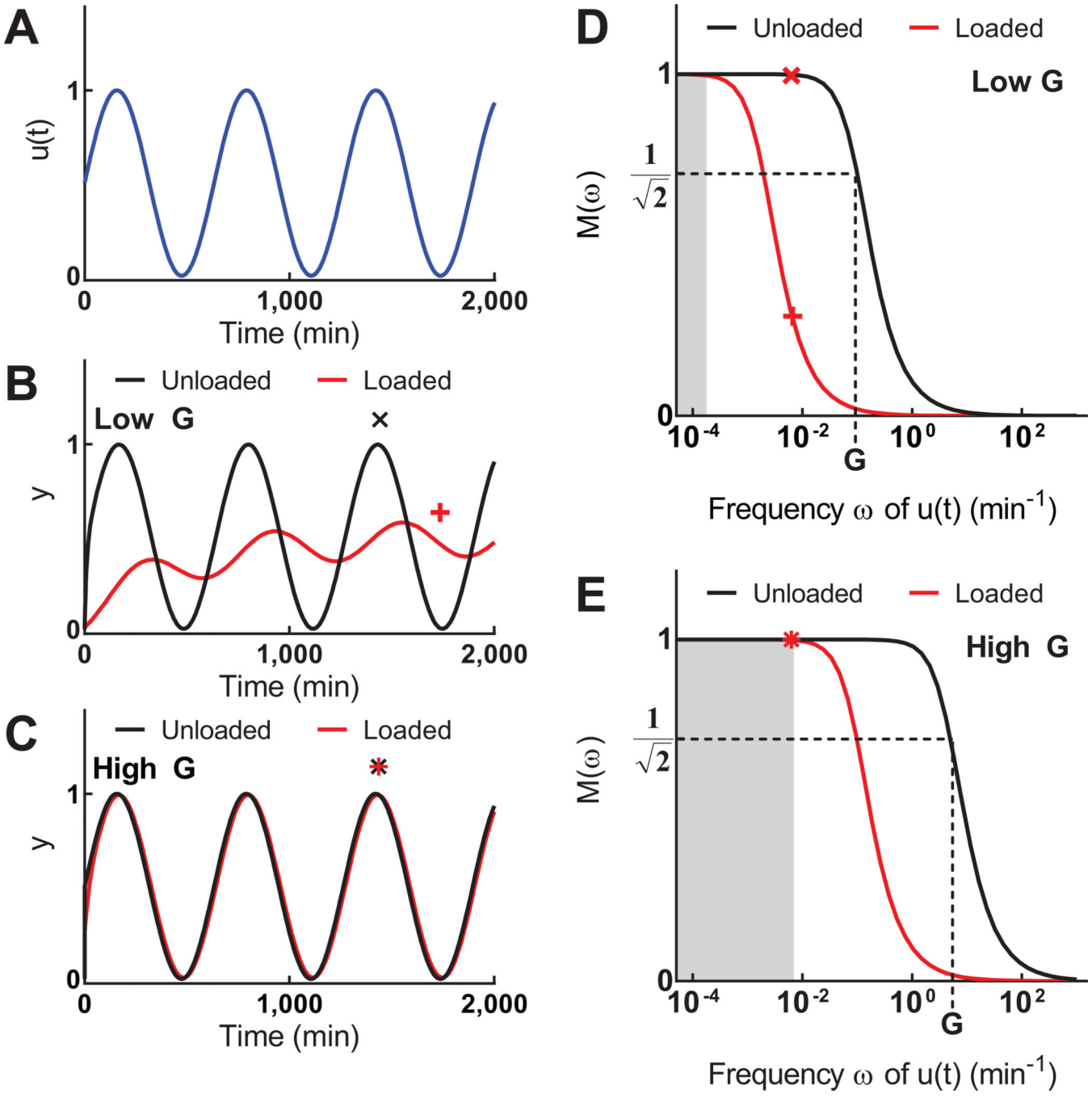

Box 1 Fig. 1. Attenuation of Retroactivity by Faster Load Driver Dynamics

(**A**) An example periodic input . (**B and C**) Simulated system responses with slow timescale (low *G*) and fast timescale (high *G*), respectively, to input in panel A. (**D and E**) Magnitude *M* as a function of the input frequency ω for a system with slow timescale (low *G*) and fast timescale (high *G*), respectively. In panels D and E, the shaded region represents the range of frequencies where retroactivity has negligible effect and this range increases with higher *G*. The bandwidth of the unloaded systems is marked by dashed lines. The magnitudes of the

oscillatory system outputs from panels B and C (input frequency in panel A) are indicated by + and ×, respectively, in panels D and E.

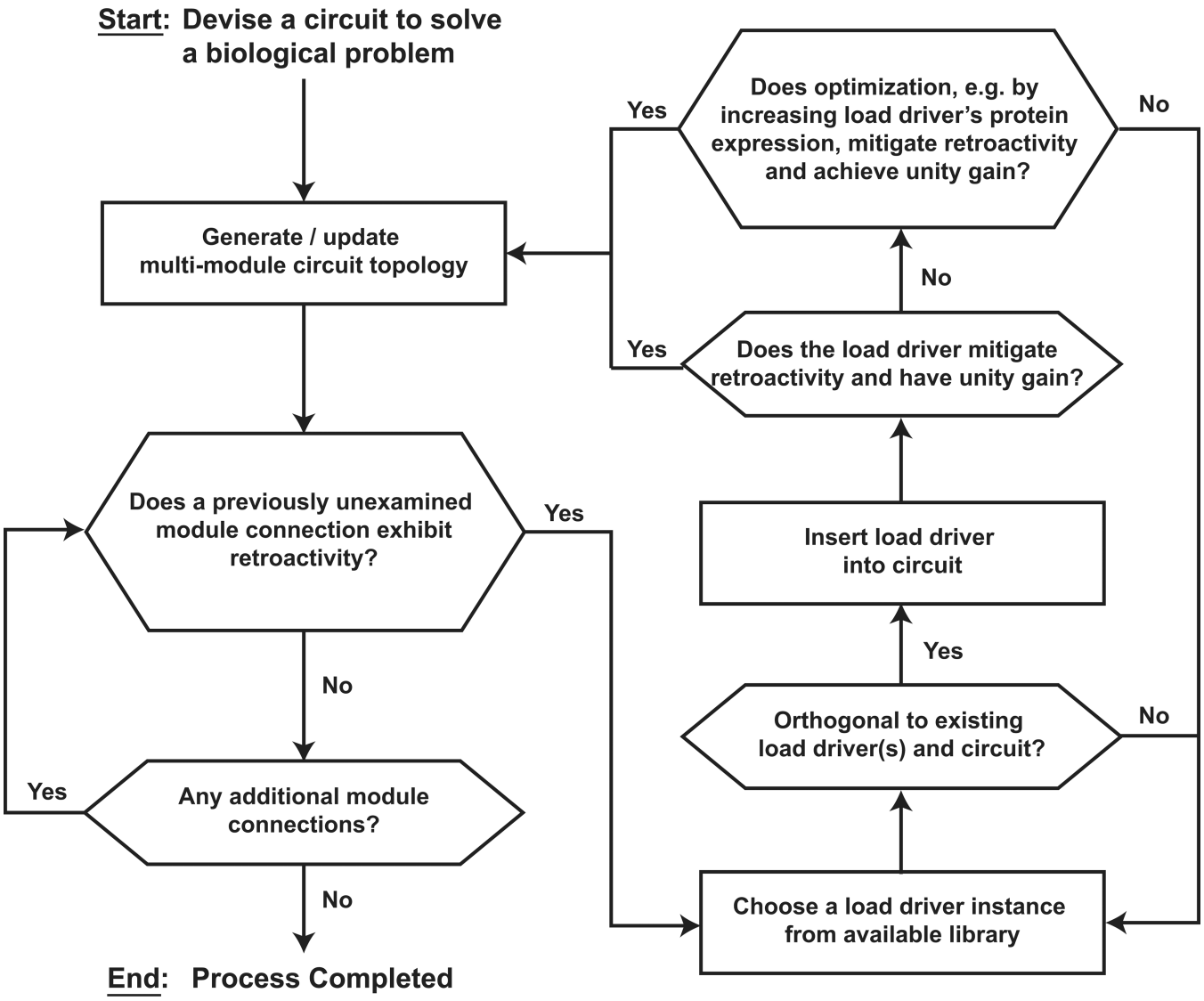

Box 2 Fig. 1.

Outline of process for integration of load drivers into synthetic circuits.

Table 1

Examples of well characterized multi-stage signaling pathways suitable for load drivers

Organism	Protein Chain	Reference
Bacillus subtilis	KinA → Spo0F → Spo0B → Spo0A	[54]
Bordetella pertussis	BvgA → BvgS → EvgA	[54]
Pseudomonas syringae	LadS → GacA → GacS	[55]
Arabidopsis thaliana	Ahk2 → Ahp1 → Arr1	[56]
Escherichia coli	TorR → TorR → TorS	[57]
Saccharomyces cerevisiae	Sln1 → Ypd1 → Skn7	[58]